

# Macroscopic quantum entanglement between an optomechanical cavity and a continuous field in presence of non-Markovian noise

S. Direkci,<sup>1,\*</sup> K. Winkler,<sup>2</sup> C. Gut,<sup>2</sup> K. Hammerer,<sup>3</sup> M. Aspelmeyer,<sup>4,5</sup> and Y. Chen<sup>1</sup>

<sup>1</sup>*Theoretical Astrophysics 350-17, California Institute of Technology, Pasadena, California 91125, USA*

<sup>2</sup>*Vienna Center for Quantum Science and Technology (VCQ),*

*Faculty of Physics & Vienna Doctoral School in Physics, University of Vienna, A-1090 Vienna, Austria*

<sup>3</sup>*Institute for Theoretical Physics and Institute for Gravitational Physics (Albert-Einstein-Institute),  
Leibniz University Hannover, Appelstrasse 2, 30167 Hannover, Germany*

<sup>4</sup>*Vienna Center for Quantum Science and Technology (VCQ),*

*Faculty of Physics, University of Vienna, A-1090 Vienna, Austria*

<sup>5</sup>*Institute for Quantum Optics and Quantum Information (IQOQI) Vienna,  
Austrian Academy of Sciences, Boltzmannngasse 3, 1090 Vienna, Austria*

(Dated: September 25, 2023)

Probing quantum entanglement with macroscopic objects allows to test quantum mechanics in new regimes. One way to realize such behavior is to couple a macroscopic mechanical oscillator to a continuous light field via radiation pressure. In view of this, the system that is discussed comprises an optomechanical cavity driven by a coherent optical field in the unresolved sideband regime where we assume Gaussian states and dynamics. We develop a framework to quantify the amount of entanglement in the system numerically. Different from previous work, we treat non-Markovian noise and take into account both the continuous optical field and the cavity mode. We apply our framework to the case of the Advanced Laser Interferometer Gravitational-Wave Observatory (Advanced LIGO) and discuss the parameter regimes where entanglement exists, even in the presence of quantum and classical noises.

## I. INTRODUCTION

Entanglement is one of the hallmarks of the “quantumness” of physical systems. Ideally, it is possible for macroscopic objects, massive and/or containing a high number of degrees of freedom, to be entangled with each other. Yet in practice, such macroscopic entanglement can be very delicate in presence of decoherence. It is an intriguing challenge to create and verify macroscopic entanglement, which is often viewed as expanding the limits of the quantum regime.

Optomechanical systems are promising candidates for experimental demonstration of macroscopic entanglement, partly due to their theoretical robustness against temperature effects [1]. They can also be used to engineer the quantum state of the mechanical system [2], where the entanglement is generated by the momentum exchange between the light reflecting from the mechanical oscillator – a phenomenon known as radiation pressure. It is theoretically well understood and broadly discussed in the literature [3–8], see for example [1, 9] for a review.

Entanglement in optomechanical devices has been widely studied and there have been several successful experimental realizations: stationary entanglement between simultaneous light tones mediated by an optomechanical device [10, 11], generation of entanglement between spaced mechanical oscillators both in the micro and macro regime via radiation pressure [12–15], and optomechanical entanglement between the light field and the mechanical oscillator in a pulsed scheme [16] are examples of such demonstrations. There also exist many proposals in the literature to further study macro-

scopic quantum phenomena in optomechanical systems [17–21] and entanglement between coupled oscillators in presence of non-Markovian baths [22]. In this work, we consider stationary optomechanical entanglement, where the system parameters (e.g. the driving), and statistical behavior thereof, are not changing over time. Schemes to verify stationary optomechanical entanglement were proposed in [4, 6, 23–25], whereas an experimental demonstration has, to our knowledge, not been performed yet.

Our system consists of a single mechanical mode interacting with an optical cavity mode and the quadratures of the light field exiting the cavity. At any time  $t$ , we study the bipartite entanglement that is present in the joint quantum state between mechanical mode, optical mode, and the light that has exited the system during  $t' \leq t$ . See Fig. 1 of Ref. [6], which includes a space-time diagram that illustrates the configuration. In the regime where the dynamics are linear, the state is Gaussian, and the noise processes are Markovian (white), the open-system optomechanical dynamics is solvable analytically and the state of the system can be known exactly [3]. The white-noise model describes well devices with high-frequency oscillators, where only thermal excitations are expected, and in the limit of large bath temperature where  $k_B T \gg \hbar \omega_m$ ,  $T$  is the temperature of the bath and  $\omega_m$  is the resonance frequency of the oscillator [26].

In this work, we extend the description to non-Markovian Gaussian noise processes where analytical results are, to our knowledge, not available, thus requiring numerical methods. This approach is applicable whenever non-white noises processes, such as structural damping [27, 28], are relevant. We extend on the methods developed in [6], incorporating a cavity, and, more importantly, non-Markovian noise processes. The technique consists in computing the minimal symplectic eigenvalue of the partially transposed covariance matrix of the

\* sdirekci@caltech.edu

system, constructed with numerical methods, which provides a measure of appropriate bipartite entanglement.

We first investigate entanglement in a generalized setting, considering a heavy suspended oscillator with a low mechanical resonance frequency. This corresponds to the free-mass limit, where the mechanical resonance frequency is much smaller than the other characteristic frequencies of the system. Then, we focus our attention on Advanced LIGO (aLIGO) [29] and use it as a case study. It has been recently shown that by injecting squeezed vacuum, the detector's quantum noise can in principle surpass the free-mass standard quantum limit (SQL) by 3 dB [30]. It is natural to ask whether this can already imply that aLIGO has built quantum entanglement between the mirrors and the light field. The answer to this question is non-trivial. First, from [30], we see that the level of classical noise is not yet below the SQL [31]. Second, the strict definition of entanglement we use here requires integrating over all frequencies: it remains uncertain whether having noise below the SQL within a certain finite frequency band automatically leads to entanglement. Therefore, we parametrize aLIGO's noise curves to investigate regimes where entanglement, according to its strict definition, exists.

This paper is organized as follows: In Sec. II, we introduce the dynamics of the system and its equations of motion. In Sec. III, we state our entanglement criterion and the covariance matrix of the system for two partitions of interest. To show the usefulness of our technique for systems with low mechanical resonance frequencies, we investigate entanglement in a generalized setting in Sec. IV. In Sec. V, we give details about aLIGO's noise budget, and talk about how we model it in our calculations. Finally, in Sec. VI, we investigate whether there is entanglement between the mechanical oscillator and the light field at aLIGO for the partitions of interest, given different parametrizations of the classical noise curves.

## II. SYSTEM DYNAMICS

Let us consider an optical cavity with a movable mirror, driven by a laser with frequency  $\omega_0$  close to one of the resonant frequencies of the cavity,  $\omega_0 + \Delta$  [32]. The quantity  $\Delta$  is often referred to as the detuning frequency of the cavity. For such a system, the linearized Hamiltonian in the interaction picture with the rotating-wave approximation (RWA) is given by [33]

$$H = \hbar\omega_m \hat{B}^\dagger \hat{B} + \hbar\Delta \hat{A}^\dagger \hat{A} - \hbar G \hat{x}(\hat{A}^\dagger + \hat{A}) + i\hbar \sqrt{2\gamma} \int_{-\infty}^{\infty} \frac{d\Omega}{2\pi} \left[ \hat{A}^\dagger \hat{c}(\omega_0 + \Omega) - \hat{A} \hat{c}^\dagger(\omega_0 + \Omega) \right] + \int_{-\infty}^{\infty} \frac{d\Omega}{2\pi} \left[ \hbar\Omega \hat{c}^\dagger(\omega_0 + \Omega) \hat{c}(\omega_0 + \Omega) \right], \quad (1)$$

where  $\hat{B}$  and  $\hat{B}^\dagger$  are the annihilation and creation operators of the mechanical mode (center of mass motion of the mirror),  $\hat{x}$  is the position of the center of mass of the mirror,  $\omega_m$  is the mechanical resonance frequency,  $\hat{A}$  and  $\hat{A}^\dagger$  are the annihilation and creation operators of the cavity mode,  $\hat{c}(\omega_0 + \Omega)$  and

$\hat{c}^\dagger(\omega_0 + \Omega)$  are the annihilation and creation operators of the external vacuum light field at frequency  $\omega_0 + \Omega$ ,  $G$  is the linear optomechanical coupling constant, and  $\gamma$  is the decay rate of the cavity mode. The position and momentum operators of the mirror are related to the creation and annihilation operators of the mechanical mode by

$$\hat{x} = \sqrt{\frac{\hbar}{M\omega_m}} \frac{(\hat{B} + \hat{B}^\dagger)}{\sqrt{2}}, \quad (2a)$$

$$\hat{p} = \sqrt{\hbar M\omega_m} \frac{(\hat{B} - \hat{B}^\dagger)}{\sqrt{2}i}. \quad (2b)$$

Note that for the sake of convenience we chose a displaced frame where all operators have zero mean. The mode operators satisfy the canonical commutation relations,

$$[\hat{A}, \hat{A}^\dagger] = [\hat{B}, \hat{B}^\dagger] = 1. \quad (3)$$

aLIGO detectors are power- and signal-recycled Fabry-Perot Michelson interferometers, which contain a high number of degrees of freedom. However, the core optomechanics can still be studied by the Hamiltonian given above; this reduction manifests itself in the “scaling-law” relations governing aLIGO's sensitivity as parameters of the signal-recycling cavity are modified [32]. From the scaling-law, the coupling constant  $G$  is related to the parameters of the interferometer by,

$$G = \sqrt{\frac{2\omega_0 P_c}{\hbar L c}}, \quad (4)$$

where  $L$  is the arm length of the interferometer (i.e. the cavity length),  $P_c$  is the power circulating inside the cavity, and  $c$  is the speed of light in vacuum.

We can transform the Hamiltonian such that the cavity mode ( $A, A^\dagger$ ) couples with the traveling wave at  $z = 0$  (where the point-wise cavity interface is located). We derive this transformation in Appendix A. We use  $\hat{u}$  and  $\hat{v}$  to label the field right before entering and right after exiting the cavity, respectively.

In this paper, we restrict ourselves to  $\Delta = 0$ . In this resonant case, the system is unconditionally stable and it reaches a steady state, in which the Heisenberg equations can be solved using Fourier transformation [34]. To write down and solve the Heisenberg equations, instead of annihilation and creation operators we use the Caves-Schumaker quadrature operators [35, 36]:

$$\hat{u}_1(\Omega) = \frac{\hat{u}(\omega_0 + \Omega) + \hat{u}^\dagger(\omega_0 - \Omega)}{\sqrt{2}}, \quad (5a)$$

$$\hat{u}_2(\Omega) = \frac{\hat{u}(\omega_0 + \Omega) - \hat{u}^\dagger(\omega_0 - \Omega)}{\sqrt{2}i}, \quad (5b)$$

where  $\hat{u}_j^\dagger(\Omega) = \hat{u}_j(-\Omega)$ . Quadratures  $\hat{v}_1(\Omega)$  and  $\hat{v}_2(\Omega)$  are defined from  $\hat{v}(\omega_0 + \Omega)$  and  $\hat{v}(\omega_0 - \Omega)$  in a similar fashion. After setting  $c = 1$ , their commutation relations are [37]

$$[\hat{u}_1(\Omega), \hat{u}_2(\Omega')] = [\hat{v}_1(\Omega), \hat{v}_2(\Omega')] = 2\pi\delta(\Omega + \Omega'), \quad (6a)$$

$$[\hat{u}_j(\Omega), \hat{u}_j(\Omega')] = [\hat{v}_j(\Omega), \hat{v}_j(\Omega')] = 0, \quad (6b)$$

for  $j = 1, 2$ . Then, in the time domain, we have

$$\hat{u}_j(t) = \int_{-\infty}^{\infty} \frac{d\Omega}{2\pi} \hat{u}_j(\Omega) e^{-i\Omega t}, \quad (7a)$$

$$[\hat{u}_1(t), \hat{u}_2(t')] = i\delta(t - t'), \quad (7b)$$

$$[\hat{u}_1(t), \hat{u}_1(t')] = [\hat{u}_2(t), \hat{u}_2(t')] = 0, \quad (7c)$$

for  $j = 1, 2$ . We similarly define quadrature operators  $\hat{A}_{1,2}$  and  $\hat{B}_{1,2}$ , in the *time domain*, with

$$\hat{A}_1(t) = \frac{\hat{A}(t) + \hat{A}^\dagger(t)}{\sqrt{2}}, \quad \hat{A}_2(t) = \frac{\hat{A}(t) - \hat{A}^\dagger(t)}{\sqrt{2}i}, \quad (8)$$

and similarly for  $\hat{B}_{1,2}$ . We also have

$$[\hat{A}_1(t), \hat{A}_1(t)] = [\hat{A}_2(t), \hat{A}_2(t)] = 0, \quad (9)$$

$$[\hat{A}_1(t), \hat{A}_2(t)] = i, \quad (10)$$

and the same for  $\hat{B}_{1,2}$ . Note here that the commutators are for same-time operators.

We include two classes of “classical” noises [37] in our system: a force noise  $\hat{n}_F$  and a sensing noise  $\hat{n}_X$ , arising from a quantum treatment of the interaction of the system with its environment. Force noise affects the center-of-mass motion of the mechanical oscillator by introducing fluctuations in its momentum. We also introduce a velocity damping of the oscillator, with a damping rate  $\gamma_m$ .  $\gamma_m$  and  $n_F$  are associated with the heat bath(s) the mass is coupled to, with the value of  $\gamma_m$  and the spectrum of  $n_F$  related by the fluctuation-dissipation theorem [38]. Sensing noise affects how the position is measured by the light field. In our model below it arises from fluctuations of the reflecting surface that introduces noise in the cavity field.

In the Heisenberg picture, the dynamics are given by the Langevin equations of motion. In the Fourier domain they are written as

$$-i\Omega \hat{A}_1 = -\gamma \hat{A}_1 + \sqrt{2\gamma} \hat{u}_1, \quad (11a)$$

$$-i\Omega \hat{A}_2 = -\gamma \hat{A}_2 + \sqrt{2\gamma} \hat{u}_2 + \sqrt{2}G(\hat{x} + \hat{n}_X), \quad (11b)$$

$$-i\Omega \hat{x} = \hat{p}/M, \quad (11c)$$

$$-i\Omega \hat{p} = -\gamma_m \hat{p} - M\omega_m^2 \hat{x} + \sqrt{2}\hbar G \hat{A}_1 + \hat{n}_F, \quad (11d)$$

$$\hat{v}_1 = \hat{u}_1 - \sqrt{2\gamma} \hat{A}_1, \quad (11e)$$

$$\hat{v}_2 = \hat{u}_2 - \sqrt{2\gamma} \hat{A}_2. \quad (11f)$$

We refer to Eqs. (11) as the Heisenberg equations for the rest of the article. It is straightforward to solve them to obtain  $(\hat{x}, \hat{p}, \hat{A}_{1,2}, \hat{v}_{1,2})$  in terms of the input fields,  $(\hat{u}_{1,2}, \hat{n}_X, \hat{n}_F)$ , referred as the input-output relations of the system. More specifically, quantum fluctuations in the in-going quadratures  $\hat{u}_{1,2}(\Omega)$  drive the system’s quantum noise [39]. From Eq. (11e) and (11f), reading the out-going field quadratures are subject to noises in  $\hat{u}_1$  and  $\hat{u}_2$ , giving rise to the *shot noise* (SN) for that readout strategy [39]. On the other hand, from Eq. (11a), we see that  $\hat{u}_1$  drives  $\hat{A}_1$ , which in Eq. (11d) drives the momentum of the test mass, which then shows up in the position of the test mass via Eq. (11c), giving rise to *quantum radiation pressure noise* (QRPN), also known as backaction noise

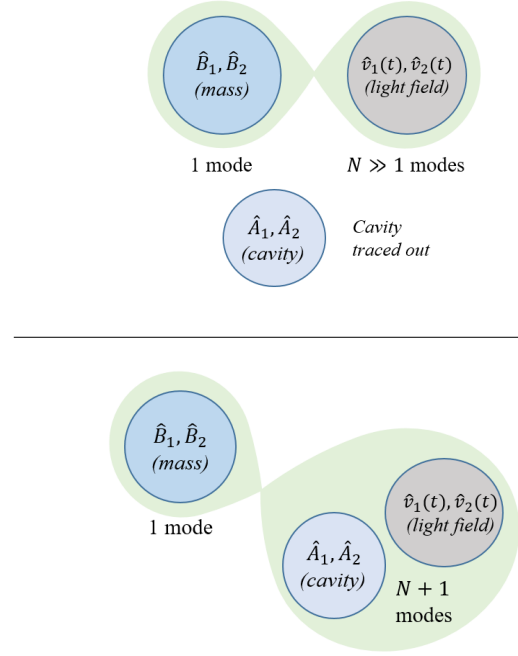


FIG. 1. Figurative representation of the two different partitions that is used while testing for entanglement, which are partitioning by tracing over (top row) and **not** tracing over (bottom row) the cavity. Note that the system configuration is not changed, i.e. cavity is still present for both partitions.

in the literature. In general, the power spectrum of the SN is inversely proportional to circulating power in the cavity, while that of the QRPN is proportional to circulating power.

### III. ENTANGLEMENT CRITERIA AND PARTITIONS

The canonical commutation relations imply that  $\mathbf{V} + \frac{1}{2}\mathbf{K}$  is positive semidefinite, where  $\mathbf{V}$  is the covariance matrix with  $V_{ij} = \langle \{\hat{X}_i - \langle \hat{X}_i \rangle, \hat{X}_j - \langle \hat{X}_j \rangle\} \rangle / 2$  and  $\mathbf{K}_{ij} = [\hat{X}_i, \hat{X}_j]$  is the commutator matrix of the quadratures in the system. This relation can be stated as

$$\mathbf{V} + \frac{1}{2}\mathbf{K} \geq 0. \quad (12)$$

Here for an  $N$ -partite system containing  $N$  harmonic oscillators, the matrices  $\mathbf{V}$  and  $\mathbf{K}$  are  $2N$ -dimensional.

To test for bipartite entanglement in a multimode system, we use the positivity of the partial transpose (PPT) criterion, which is necessary and sufficient to test for the separability of one of the modes from the rest for Gaussian systems [40–42]. To use the PPT criterion in this context, one obtains the partial-transposed covariance matrix  $\mathbf{V}_{\text{pt}}$  by reverting the momentum of that one mode (which puts a minus sign on the column and the row that contains the momentum in question) [43]. The PPT criterion for separability is expressed as

$$\mathbf{V}_{\text{pt}} + \frac{1}{2}\mathbf{K} \geq 0 \Leftrightarrow \text{Separability}. \quad (13)$$

The amount of entanglement is quantified by the logarithmic negativity,  $E_N$  [44]. For a Gaussian state of  $N$  modes, it is defined as

$$E_N = \sum_{j=1}^N \max\{0, -\log_2(\tilde{v}_j)\}, \quad (14)$$

where  $\tilde{v}_j$ ,  $j = 1, \dots, N$  are the symplectic eigenvalues of the partially transposed covariance matrix,  $\mathbf{V}_{\text{pt}}$ , which are given by the absolute values of the eigenvalues of  $\mathbf{K}^{-1}\mathbf{V}_{\text{pt}}$ . For 1 vs.  $N-1$  mode partitions, only one of the symplectic eigenvalues of  $\mathbf{V}_{\text{pt}}$  can have a magnitude smaller than 1 [45], therefore there can be at most one negative eigenvalue of  $\mathbf{V}_{\text{pt}} + \frac{1}{2}\mathbf{K}$ . We label the corresponding symplectic eigenvalue as  $\tilde{v}_{\min}$ .

Using the PPT criterion, we test for entanglement between the mechanical oscillator and the optical field in two ways: first, we construct the covariance matrix  $\mathbf{V}$  with the mechanical mode and the modes of the light field, essentially tracing out the cavity mode. Here, we perform the partial transpose operation with respect to the mechanical oscillator. Second, we include the cavity mode in the covariance matrix while still taking the partial transpose with respect to the mechanical oscillator, which corresponds to measuring the entanglement between the oscillator and the joint system of the cavity plus external light field. The two ways of partitioning are depicted in Fig. 1. The elements of the covariance matrix  $\mathbf{V}$  for both types of partitions, as well as the discretization of  $\mathbf{V}$  can be found in Appendix D.

#### IV. ENTANGLEMENT IN PRESENCE OF NON-MARKOVIAN NOISES

Due to the numerical nature of the algorithm, we can tackle any noise spectral density associated with  $\hat{u}_1(\Omega)$ ,  $\hat{u}_2(\Omega)$ ,  $\hat{n}_F(\Omega)$  and  $\hat{n}_X(\Omega)$  using the PPT criterion defined in Eq. (13) to determine whether entanglement is present for a given partition. Conversely, this problem is analytically solvable only for some simplified noise models to our knowledge, such as assuming all the noise sources to have a white spectrum [6, 23].

To show the usefulness of the method, we investigate entanglement in heavy suspended oscillators with relatively low mechanical resonance frequencies. For such systems, the mechanical resonance frequency,  $\omega_m$ , is much smaller than the other frequencies of the system, which is referred to as the *free-mass limit*. In this setting,  $\omega_m$  essentially does not affect the dynamics. Furthermore, in this limit where  $\Omega \gg \omega_m, \gamma_m$ , the tradeoff between shot noise and QRPN give rise to the SQL [46], given by

$$S_{\text{SQL}}(\Omega) = \frac{2\hbar}{M\Omega^2}. \quad (15)$$

In the context of suspended oscillators,  $\hat{n}_F(\Omega)$  is the force that gives rise to the suspension thermal noise, whereas  $\hat{n}_X(\Omega)$  is an effective displacement that gives rise to coating thermal noise. When thermal noise is due to the internal friction of the suspension or the oscillator, the noise spectrum of  $\hat{n}_F(\Omega)$  and

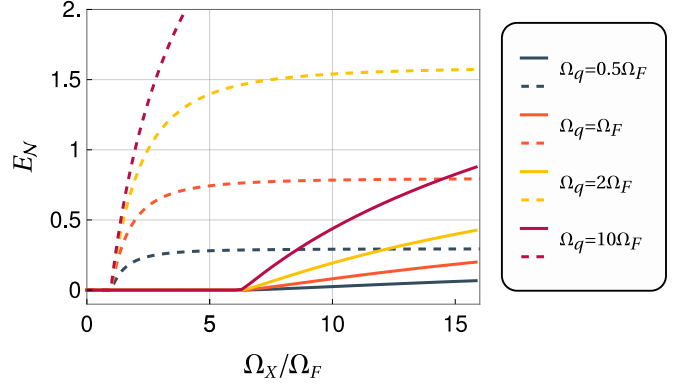


FIG. 2. Logarithmic negativity between the mechanical oscillator and the outgoing light field in the free mass limit as a function of  $\Omega_X/\Omega_F$  for various  $\Omega_q/\Omega_F$ . We plot the results for Markovian and non-Markovian force and sensing noise with dashed and plain lines respectively. Note that entanglement does not exist for  $\Omega_X/\Omega_F \lesssim 1$  with Markovian and for  $\Omega_X/\Omega_F \lesssim 6.3$  with non-Markovian noise sources, for  $\omega_m/(2\pi) = 1$  Hz,  $\gamma_m/(2\pi) = 0.01$  Hz, and a cutoff frequency of  $\Omega_c/(2\pi) = 0.001$  Hz.

$\hat{n}_X(\Omega)$  decrease as  $1/\Omega$  above internal resonances, which is referred to as *structural damping* [47–49]. Evidently, structural damping gives rise to non-Markovian noises, and the position-referred noise spectral densities of  $\hat{n}_F(\Omega)$  and  $\hat{n}_X(\Omega)$  are given, in the free-mass limit, by

$$S_F(\Omega) = \frac{2\hbar}{M} \frac{\Omega_F^3}{|\Omega|^5}, \quad (16a)$$

$$S_X(\Omega) = \frac{2\hbar}{M} \frac{1}{\Omega_X |\Omega|}, \quad (16b)$$

where  $\Omega_F$  and  $\Omega_X$  are the frequencies where the respective noise curves cross the SQL, given in Eq. (15). Accordingly, they encode the strength of the noise processes  $n_F$  and  $n_X$ , relative to the SQL level. For  $\hat{n}_F(\Omega)$ , the position-referred spectrum is related to the noise spectral density, labeled as  $S_{n_F}(\Omega)$ , with  $S_F(\Omega) = S_{n_F}(\Omega)/M^2\Omega^4$ . Whereas for  $\hat{n}_X(\Omega)$ , the position-referred spectrum  $S_X(\Omega)$  is also the noise spectral density  $S_{n_X}(\Omega)$  [50]. The incoming field quadratures  $\hat{u}_j$  have uncorrelated white spectra given by Eq. (D8), since we assume the incoming field to be at vacuum state.

We list some relevant experiments with low mechanical oscillation frequencies in Table I. Note that large scale experiments such as aLIGO, KAGRA [52], and VIRGO [53] are subject to seismic noise in addition to thermal noises, which usually does not follow structural damping and is disregarded in calculating  $\Omega_F$  for this Table. Seismic noise imposes further challenge upon reaching entanglement, which is explained in detail in Sec. VI A.

In the limit of large cavity bandwidth,  $\gamma \gg \Omega$  the cavity can be eliminated adiabatically. Then, the equations of motion in

TABLE I. Relevant Experiments

Experiments	$\omega_m/(2\pi)$	$\Omega_F/(2\pi)$	$\Omega_X/(2\pi)$	$\Omega_q/(2\pi)$	$\Omega_X/\Omega_F$
LIGO	1	10	50	60	5
KAGRA	1	40	300	80	8
VIRGO	1	10	40	50	4

(11) are modified as

$$\hat{v}_1(\Omega) = \hat{u}_1(\Omega), \quad (17a)$$

$$\hat{v}_2(\Omega) = \hat{u}_2(\Omega) + \alpha(\hat{x}(\Omega) + \hat{n}_X(\Omega)), \quad (17b)$$

$$-i\Omega\hat{p}(\Omega) = -\gamma_m\hat{p}(\Omega) - M\omega_m^2\hat{x}(\Omega) + \hbar\alpha\hat{u}_1(\Omega) + \hat{n}_F(\Omega), \quad (17c)$$

$$-i\Omega\hat{x}(\Omega) = \hat{p}(\Omega)/M, \quad (17d)$$

where  $\alpha = \Omega_q \sqrt{M/\hbar}$  and  $\Omega_q = 2G \sqrt{\hbar/M\gamma}$  is the characteristic interaction frequency. We fix  $\omega_m/(2\pi) = 1$  Hz,  $\gamma_m/(2\pi) = 0.01$  Hz,  $\Omega_F/(2\pi) = 100$  Hz and vary  $\Omega_X$  and  $\Omega_q$ . Note that the aim of these choices is to ensure that  $\Omega_F \gg \omega_m \gg \gamma_m$ , i.e. that the free-mass limit is justified and we are in the large mechanical quality factor regime. Furthermore,  $\Omega_F \gg \omega_m$  implies the large bath temperature limit where  $k_B T \gg \hbar\omega_m$ ,  $T$  being the temperature of the bath. Lastly,  $\Omega_q \gg \omega_m$  ensures that the measurement of the system performed by light is faster than the dynamics of the system.

Since we work in the free-mass limit, the relevant parameters on which the presence of entanglement depends are  $\Omega_q$ ,  $\Omega_F$ , and  $\Omega_X$ . In this limit, scaling all of them by the same constant factor does not have an effect on the resulting dynamics. Therefore, we define the unitless ratios  $\Omega_q/\Omega_F$  and  $\Omega_X/\Omega_F$ , which describe the system fully, in this limit. Note that the amount of classical noises in the system decreases with increasing  $\Omega_X/\Omega_F$ .

We look for entanglement between the oscillator and the outgoing light field by varying the ratio  $\Omega_X/\Omega_F$  for various  $\Omega_q$  in Fig. 2 and we plot the results with plain lines. We find that entanglement does not exist for  $\Omega_X/\Omega_F \lesssim 6.3$  for any value of  $\Omega_q$ . For  $\Omega_X/\Omega_F \gtrsim 6.3$ , the system is entangled for any (finite)  $\Omega_q$ , and the entanglement increases monotonously with increasing  $\Omega_X/\Omega_F$ . This implies the existence of “universal” entanglement, meaning that whether the system is entangled or not is independent from  $\Omega_q$ , the interaction frequency (or, in other words, how fast the system is measured by light). When the system is entangled, the amount of entanglement increases when  $\Omega_q$  is increased. We also note that the threshold for  $\Omega_X/\Omega_F$  above which the system is entangled depends on the low-frequency cutoff  $\Omega_c$  chosen in our model for the spectra of  $n_F$  and  $n_X$ . Here, our model is in the form  $1/(\Omega + \Omega_c)$  with  $\Omega_c/(2\pi) = 0.001$  Hz for both force and the sensing noises, such that the average noise power at DC is  $1/\Omega_c = 1000/(2\pi)$  s. We saw that the threshold is inversely proportional to the cutoff frequency.

In order to see the significance of non-Markovianity on the results, we repeat the same procedure with a white force and sensing noise. The noise spectra are given by  $S_{n_F}(\Omega) = 2\hbar M \Omega_F^2$ ,  $S_F(\Omega) = 2\hbar \Omega_F^2 / M \Omega^4$ , and  $S_{n_X}(\Omega) = S_X(\Omega) =$

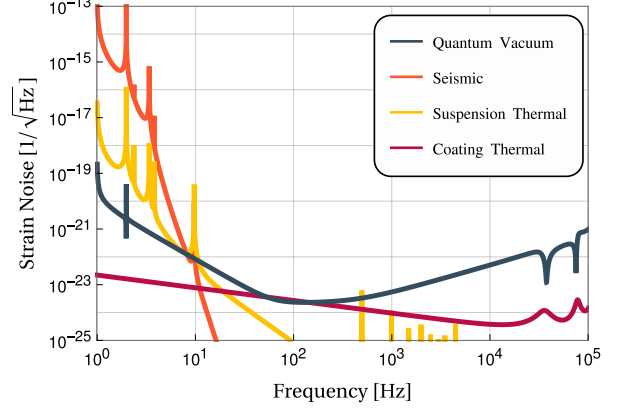


FIG. 3. aLIGO noise budget obtained from pygwinc. Only the dominant classical noise sources are plotted, along with the quantum noise. The total force noise in the system is the sum of the seismic noise and the suspension thermal noise, which is effective at low frequencies. The coating Brownian thermal noise is taken as the main constituent of the sensing noise. As can be seen from the figure, quantum noise dominates over the sensing noise by a large margin at high frequencies.

$2\hbar/M\Omega_X^2$ . The results can again be found in Fig. 2, plotted with dashed lines, where the system is not entangled for any  $\Omega_q$  when  $\Omega_X/\Omega_F \lesssim 1$ , whereas for  $\Omega_X/\Omega_F \gtrsim 1$ , entanglement exists for all  $\Omega_q$  and the amount of entanglement increases with increasing  $\Omega_q$ . Since we see this behavior for both Markovian and non-Markovian noise, we conjecture that the universality of the entangling-disentangling phase transition is independent of the power spectral densities of the classical noises, and that the power spectral densities only determine the threshold above which we have entanglement for all  $\Omega_q$ .

## V. NOISE MODEL OF ALIGO

The primary noise sources in aLIGO, other than the quantum noise, are the following [29]: seismic noise and suspension thermal noise are the main constituents of the force noise, and mirror coating thermal noise constitutes the sensing noise. The noise spectrum is dominated by seismic and thermal noise at low frequencies (until 100 Hz), and quantum noise at high frequencies, cf. Fig. 3. The interferometer noise is stationary and Gaussian to very good approximation in absence of glitches (i.e. transient noise artifacts) [54].

Seismic noise occurs because of the ground motion at the interferometer sites. This motion is  $\sim 10^{-9}\text{m}/\sqrt{\text{Hz}}$  at 10

Hz [55]. To provide isolation from this motion, the mirrors are suspended from quadruple pendulums [56]. The primary components of thermal noise are suspension thermal noise and coating Brownian noise. Suspension thermal noise occurs due to loss in the fused silica fibres used in the final suspension stage [29], whereas the coating Brownian noise (which is classified as a sensing noise) occurs due to the mechanical dissipation in the coatings [57]. Other types of sensing noise comprises of many noise sources that are dominant at high frequencies, such as thermal fluctuations of the mirror's shape, optical losses, or photodetection inefficiency [58]. The noise budget of aLIGO can be found in Figure 3.

Due to the classification above, we represent the sum of the seismic and the suspension thermal noise with  $\hat{n}_F(\Omega)$ , and the coating thermal noise with  $\hat{n}_X(\Omega)$ . We use the aLIGO noise budgets as given by the Python Gravitational Wave Interferometer Noise Calculator library (pygwinc) [59] and model them with rational functions of  $\Omega^2$ . The noise spectra are modelled by

$$S_F^{LIGO}(\Omega) = \frac{\tau_F \alpha_{F_1}}{\left(\frac{\Omega}{\omega_F} \alpha_{F_2}\right)^{14} + 1}, \quad (18a)$$

$$S_X^{LIGO}(\Omega) = \tau_{X_1} \left(\frac{\Omega}{\omega_X}\right)^2 \alpha_{X_1} + \tau_{X_2} \alpha_{X_2}, \quad (18b)$$

where  $S_F^{LIGO}(\Omega)$  is the spectrum of the force noise and  $S_X^{LIGO}(\Omega)$  is the spectrum of the sensing noise. We model  $S_F^{LIGO}(\Omega)$  to decay as  $\Omega^{-14}$  instead of  $\Omega^{-16}$  (which is the expected behavior for quadruple suspension systems) since it performs better at approximating the global behavior. The power spectral densities are characterized by the time constants  $\tau_F$ ,  $\tau_{X_1}$ ,  $\tau_{X_2}$  and cutoff frequencies  $\omega_F$ ,  $\omega_X$ . The values of these parameters can be found in Appendix B, Table II.  $\alpha_{F_1}$ ,  $\alpha_{F_2}$ ,  $\alpha_{X_1}$ , and  $\alpha_{X_2}$  are dimensionless constants that will be used to change the noise curves in Section VI. Their effect on the noise curves can be seen in Fig. 4. If we set all of them to be unity, we get our model of aLIGO noise curves.

Even though the parameters of aLIGO are well-known, they need to be recomputed since we are reducing the antisymmetric mode of the interferometer to a single cavity. The relation between the parameters of the antisymmetric mode and the parameters of the reduced cavity have already been computed [32], however, we choose to work numerically and find the parameters of the reduced cavity  $G$ ,  $\gamma$ ,  $M$ ,  $\gamma_m$ ,  $\omega_m$ , and  $L$  by fitting aLIGO's quantum noise spectrum found in pygwinc. The modeled classical and quantum noise curves can be found in Appendix C, Fig. C.1. The fitted parameters can be found in Appendix B, Table III.

## VI. ENTANGLEMENT IN aLIGO

In aLIGO, the spectrum is dominated by force noise for low frequencies and quantum noise for high frequencies, therefore we expect the sensing noise to not affect the entanglement significantly, which we observed with our numerics. Then, we focus on the effect of the force noise on the entanglement and

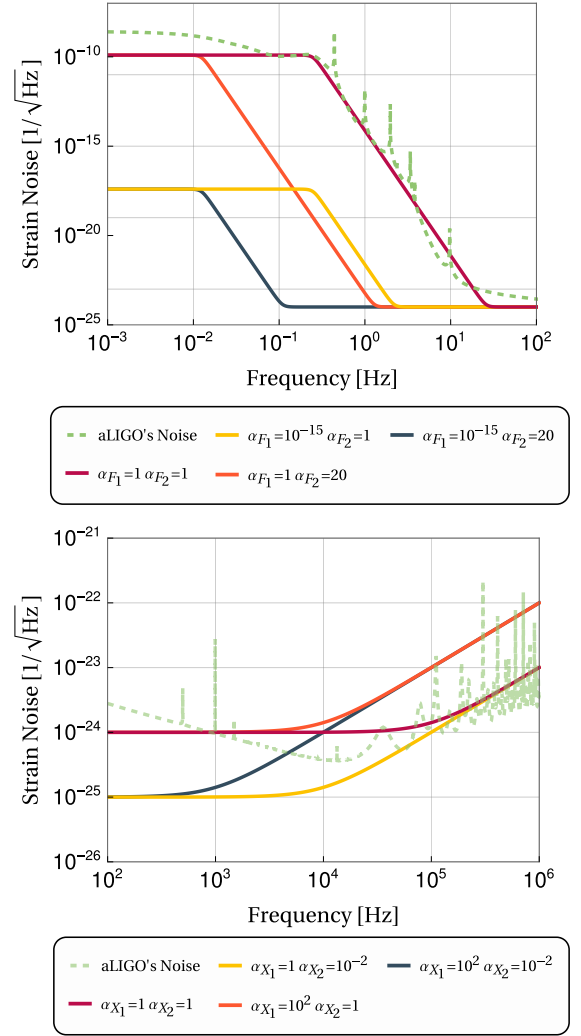


FIG. 4. Force (top row) and sensing noise (bottom row) spectra parametrized by  $\alpha_{F_1}$ ,  $\alpha_{F_2}$ ,  $\alpha_{X_1}$ , and  $\alpha_{X_2}$ . The effect of  $\alpha_{F_1}$  is to rise and lower the nominal noise strength below the cutoff frequency and  $\alpha_{F_2}$  shifts the cutoff frequency. Similarly,  $\alpha_{X_1}$  shifts the cutoff frequency where the sensing noise starts increasing as  $\Omega^2$ , whereas  $\alpha_{X_2}$  shifts the nominal noise level.

use the parameters  $\alpha_{F_1}$  and  $\alpha_{F_2}$  to modify the force noise spectrum, and set  $\alpha_{X_1} = \alpha_{X_2} = 1$  throughout all of the following subsections. We also introduce resonant modes to investigate the system as accurately as possible. Intuitively, we expect the entanglement to be destroyed in presence of high classical noise levels.

### A. Effect of Force Noise

First, we investigate the effect of the force noise spectrum on entanglement and we calculate the logarithmic negativity  $E_N$  as a function of  $\alpha_{F_1}$  and  $\alpha_{F_2}$ , for both of the partitions described in Sec. III. For all pairs  $\alpha_{F_1}$  and  $\alpha_{F_2}$  here, we find larger logarithmic negativity values when we do not trace over the cavity. The results for the partition where we do not trace



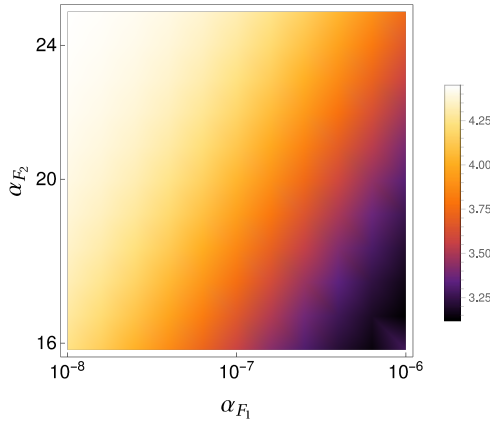


FIG. 5. The effect of the force noise spectrum on the logarithmic negativity when we do not trace over the cavity. Note that the force noise levels increase toward the bottom-right of the figure and our fit of aLIGO's operation regime is for  $\alpha_{F_1} = \alpha_{F_2} = 1$ .

over the cavity can be found in Fig. 5. The amount of entanglement in the system diminishes when the force noise increases: that is towards the bottom-right of the plot where  $\alpha_{F_1}$  increases (proportional to the DC noise power) and  $\alpha_{F_2}$  decreases (inversely proportional to the noise bandwidth), cf. Sec. V and Fig. 4. Our fit of aLIGO's force noise level is for  $\alpha_{F_1} = \alpha_{F_2} = 1$ , hence this plot is for comparatively low level of force noise. Further to the bottom-right, the numerics become unstable and do not converge due to the wide range of orders of magnitude entering the calculation; see Appendix E for a discussion of the numerical implementation. Therefore, we cannot not give a definite answer about optomechanical entanglement in aLIGO with our model yet.

Next, we look for entanglement in the absence of the seismic noise, since it is the dominating contribution to the force noise of the system. Not being subjected to seismic noise is a realistic scenario for space-based gravitational-wave interferometers, such as the Laser Interferometer Space Antenna (LISA) [60]. For aLIGO, in absence of seismic noise, suspension thermal noise dominates the spectrum for low frequencies, which is modelled as

$$S_{ST}(\Omega) = \frac{\tau_{ST}}{\left(\frac{\Omega}{\omega_{ST}}\right)^8 + 1}, \quad (19)$$

similar to how the total force noise was modelled in Sec. V. The parameters  $\tau_{ST}$  and  $\omega_{ST}$  can be found in Table II. Without changing the other parameters in the system, we find that we can achieve negativities of 1.52 and 1.72 for the partitions where we do and do not trace over the cavity respectively. This means that, in the absence of seismic noise, aLIGO has stationary optomechanical entanglement in its current operating regime.

### B. Effect of Low Frequency Resonances

Both the classical and the quantum noise curves contain many resonances, as can be seen from Fig. 3. The resonances

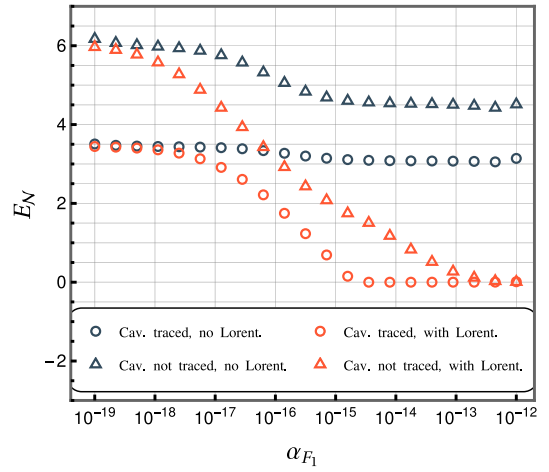


FIG. 6. The effect of resonant modes on the logarithmic negativity,  $E_N$ , for both partitions. We see that the negativity reduces with increasing  $\alpha_{F_1}$  or with the introduction of resonant modes. Note that  $\alpha_{F_2} = 1$ .

in the seismic and suspension thermal noise arise from the displacement noises of the rigid-body resonant modes of the 4-stage suspension system [56]. These modes can be modeled with a sum of Lorentzians multiplying the force noise spectrum defined in Eq. (18). Then, the new formula defining the spectrum of the force noise is given as

$$S_F^R(\Omega) = \frac{\tau_F \alpha_{F_1}}{\left(\frac{\Omega}{\omega_F} \alpha_{F_2}\right)^{14} + 1} \left(1 + \sum_i \frac{A_{v_i}^2}{(\Omega - \Omega_{v_i})^2 + (\frac{1}{2}\Gamma_{v_i})^2}\right) \quad \text{with } \Omega > 0, \quad (20a)$$

$$S_F^R(\Omega) = S_F^R(-\Omega), \quad (20b)$$

where the sum is over the resonant modes. The parameters  $\Omega_{v_i}$ ,  $\Gamma_{v_i}$ , and  $A_{v_i}$  are the mode frequencies, full widths at half maximum (FWHM), and the amplitudes of the Lorentzians respectively, and are listed in Appendix B, Table IV for the modes with the biggest relative amplitudes.

We investigate the effect of the resonant modes on the entanglement. In Fig. 6, with low force noise guarantying well-behaved numerics and setting  $\alpha_{F_2} = 1$ , we plot  $E_N$  for noise curves with and without these modes (orange and gray, resp.) and for both partitions (circles when the cavity is traced out). We see explicitly here that there is more entanglement in the partition where we do not trace over the cavity. For low noise (low  $\alpha_{F_1}$ ), the negativity remains unchanged, hence the resonant modes do not affect the entanglement significantly in this regime. As the level of noise increases, resonant modes cause the logarithmic negativity to decrease faster than the negativities calculated without the resonant modes for both partitions. The system becomes separable when resonant modes are included for  $\alpha_{F_1} \approx 10^{-15}$  and  $\alpha_{F_1} \approx 10^{-12}$  when we do and do not trace over the cavity respectively. It seems reasonable to expect that entanglement will not emerge when force noise

becomes stronger. Hence, extrapolating  $\alpha_{F_1} \rightarrow 1$ , this is evidence (but not a rigorous proof) that aLIGO in its current operation regime (but without squeezed input) probably contains no optomechanical entanglement.

## VII. CONCLUSIONS

In this paper, we developed a framework to determine and quantify bipartite entanglement in an optomechanical system in the non-sideband-resolved regime, in presence of non-Markovian Gaussian noises. The main novelty of our work is to enable the study of non-Markovian noise drives, which are common in devices with low mechanical frequencies, typically associated with large/macroscopic masses. Hence, we focused on macroscopic entanglement and used a free mass with structural damping and coating Brownian noise as an initial example, and then aLIGO as a more detailed case study.

We tested for bipartite entanglement by looking at the separability between the mechanical oscillator and (i) the outgoing light field, (ii) the joint system of the cavity and the outgoing light field. For low levels of classical noise, we saw that the latter partition is more entangled compared to the former. However, for high levels of classical noise, we did not see a significant advantage in using one partition over the other.

In the low mechanical frequency regime, where the free-mass limit approximation holds, we found that the presence of entanglement is independent of the coherent optomechanical interaction strength and depends only on the relative strength of force and sensing noise. This result is similar to that already found in [4] for white noise drive. Furthermore, by parametrizing the noise curves of aLIGO, we were able to find a region of noise curves where entanglement exists, and we showed that there is a trade-off between the overall noise level and the cutoff frequency. Due to the high level of the current classical noise in aLIGO, we were not able to reach a definite conclusion in terms of the existence of entanglement in the system, even though it's unlikely to have a significant amount of entanglement based on our simulations. However, we saw that entanglement exists if we assume a system without seismic noise, even when the suspension thermal noise is still present. This is an important result since it shows that classical noises, even at very low frequencies, are able to demolish entanglement.

We also looked at how resonances in the noise curves of the system affect the amount of entanglement, and saw that entanglement is more resistant (i.e. it disappears for higher levels of classical noise) for the partition where we test for the separability between the mechanical oscillator and the joint system of the cavity and the outgoing light field. For future work, we plan to develop better sampling strategies to overcome numerical instabilities.

## ACKNOWLEDGMENTS

We thank the Chen Quantum Group for helpful discussions. S.D. and Y.C. acknowledge the support by the Simons Foun-

ation (Award Number 568762). K.W., C.G., and M.A. received funding from the European Research Council (ERC) under the European Union's Horizon 2020 research and innovation program (grant agreement No 951234), and from the Research Network Quantum Aspects of Spacetime (TURIS). K.H. was supported by the Deutsche Forschungsgemeinschaft (DFG, German Research Foundation) through Project-ID 274200144 – SFB 1227 (projects A06) and Project-ID 390837967 - EXC 2123.

## Appendix A: Transformation of the Optomechanical Hamiltonian

Strictly speaking, the Hamiltonian in Eq. (1) is written in terms of Schrödinger operators. The symbol  $\Omega$  in Eq. (1) is used to label a spatial mode which has a reduced wavenumber of  $\Omega/c$ , and a free oscillation frequency of  $\Omega$ . More specifically,  $\omega_0 + \Omega$  is used to indicate a spatial mode whose wave number is  $(\omega_0 + \Omega)/c$ , where  $c$  is the speed of light. We can also write the same Hamiltonian in the spatial domain. Following [33] and setting  $c = 1$ , we define

$$\hat{c}(z) = \int_{-\infty}^{\infty} \frac{d\Omega}{2\pi} \hat{c}(\omega_0 + \Omega) e^{i\Omega z}, \quad (\text{A1})$$

which represents a spatial mode of the light field with wave number  $\Omega$  — or a temporal mode of the free light field with frequency  $\Omega$ , since we assume no dispersion. The Hamiltonian can then be rewritten as

$$\begin{aligned} H = & \hbar\omega_m \hat{B}^\dagger \hat{B} + \hbar\Delta \hat{A}^\dagger \hat{A} - \hbar G \hat{x}(\hat{A}^\dagger + \hat{A}) \\ & + i\hbar \sqrt{2\gamma} [\hat{A}^\dagger \hat{c}(z=0) - \hat{A} \hat{c}^\dagger(z=0)] \\ & - i\hbar \int_{-\infty}^{\infty} \hat{c}^\dagger(z) \partial_z \hat{c}(z) dz. \end{aligned} \quad (\text{A2})$$

The only non-zero commutators for the creation and annihilation operators, as well as the spatial modes of the light field are

$$[\hat{c}(\omega_0 + \Omega), \hat{c}^\dagger(\omega_0 + \Omega')] = 2\pi\delta(\Omega - \Omega'), \quad (\text{A3a})$$

$$[\hat{c}(z), \hat{c}^\dagger(z')] = \delta(z - z'), \quad (\text{A3b})$$

where  $\delta$  is the Dirac delta distribution.

## Appendix B: Parameter Tables

This appendix contains the tables with the numerical values of the parameters used in modelling the classical and quantum noise curves, including the resonant modes. The parameters were calculated by minimizing the mean squared error between the actual noise curves of aLIGO taken from pygwinc and the theoretical models, characterized by the parameters of interest, sampled logarithmically in frequency. Table II contains the parameters for the classical force and sensing noise in aLIGO defined in Eqs. (18), Table III contains the parameters of aLIGO introduced in the optomechanical Hamiltonian



of Sec. II, and lastly, Table IV contains the parameters of the resonant modes present in aLIGO's noise curves, modeled with Eq. (20).

TABLE II: Classical Noise Model Parameters

Parameter	Symbol	Value	Units
Force Noise Time Constant	$\tau_F$	$1.6 \cdot 10^{-20}$	s
Force Noise Cutoff Frequency	$\omega_F$	$2\pi \cdot 0.25$	rad/s
Sensing Noise Time Constant 1	$\tau_{X_1}$	$10^{-50}$	s
Sensing Noise Time Constant 2	$\tau_{X_2}$	$10^{-48}$	s
Sensing Noise Cutoff Frequency	$\omega_X$	$2\pi \cdot 10^4$	rad/s
Suspension Thermal Noise Time Constant	$\tau_{ST}$	$3.1 \cdot 10^{-35}$	s
Suspension Thermal Noise Cutoff Frequency	$\omega_{ST}$	$2\pi \cdot 1.9 \cdot 10^3$	rad/s

TABLE III: aLIGO Parameters

Parameter	Symbol	Value	Units
Mechanical Resonant Frequency	$\omega_m$	$2\pi \cdot 0.9991$	rad/s
Mirror Mass	$M$	9.446	kg
Cavity Decay Rate	$\gamma$	$2\pi \cdot 424.6$	rad/s
Arm Length	$L$	3.995	km
Circulating Power	$P_c$	322.7	kW
Laser Wavelength	$\lambda$	1064	nm
Mechanical Damping	$\gamma_m$	$2\pi \cdot 10^{-3}$	rad/s

TABLE IV: Resonant Mode Parameters

Parameter	Symbol	Value	Units
Mode Frequency	$\Omega_{v_1}$	$2\pi \cdot 0.441$	rad/s
	$\Omega_{v_2}$	$2\pi \cdot 0.995$	rad/s
	$\Omega_{v_3}$	$2\pi \cdot 1.98$	rad/s
	$\Omega_{v_4}$	$2\pi \cdot 2.37$	rad/s
	$\Omega_{v_5}$	$2\pi \cdot 3.38$	rad/s
	$\Omega_{v_6}$	$2\pi \cdot 3.81$	rad/s
	$\Omega_{v_7}$	$2\pi \cdot 9.73$	rad/s
Full Width at Half Maximum	$\Gamma_{v_1}$	$2\pi \cdot 1.92 \cdot 10^{-3}$	rad/s
	$\Gamma_{v_2}$	$2\pi \cdot 5.63 \cdot 10^{-5}$	rad/s
	$\Gamma_{v_3}$	$2\pi \cdot 2.11 \cdot 10^{-5}$	rad/s
	$\Gamma_{v_4}$	$2\pi \cdot 1.44 \cdot 10^{-1}$	rad/s
	$\Gamma_{v_5}$	$2\pi \cdot 1.45 \cdot 10^{-4}$	rad/s
	$\Gamma_{v_6}$	$2\pi \cdot 1.65 \cdot 10^{-3}$	rad/s
	$\Gamma_{v_7}$	$2\pi \cdot 1.03 \cdot 10^{-3}$	rad/s
Amplitude	$A_{v_1}$	159	rad/s
	$A_{v_2}$	93.8	rad/s
	$A_{v_3}$	538	rad/s
	$A_{v_4}$	235	rad/s
	$A_{v_5}$	353	rad/s
	$A_{v_6}$	27.4	rad/s
	$A_{v_7}$	78.0	rad/s

### Appendix C: Noise Model

Our model for the total classical and quantum noise in aLIGO is displayed in Fig. C.1. Note that the coating Brownian noise, which is the dominating classical noise source

above  $\sim 10$  Hz, is modeled in a piecewise manner: a white noise in the  $10 - 10^5$  Hz band and a noise source increasing as  $\Omega^2$  for frequencies larger than  $10^5$  Hz. Even though the sensing noise in the  $10 - 10^5$  Hz band decreases as  $\Omega^{0.8}$  in the power spectral density, we choose to model it with a frequency-independent white noise for simplified calculations. Our choice is justified since the quantum noise dominates over the coating Brownian noise in that region.

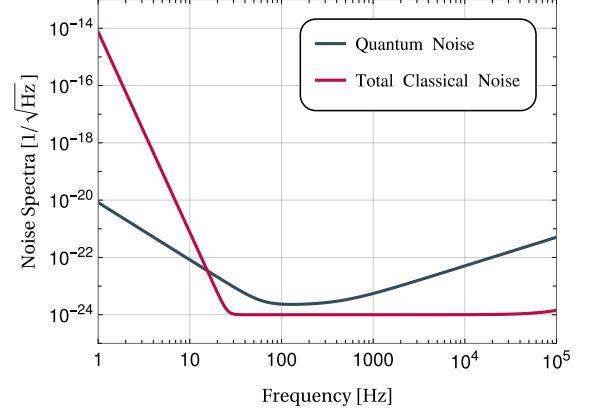


FIG. C.1. Modeled noise spectrum for aLIGO.

### Appendix D: Structure of the Covariance Matrix

The mirror and the cavity, at  $t = 0$ , constitute two modes, whereas there is an infinite number of modes in the outgoing light field given by the quadratures  $\hat{v}_1(t), \hat{v}_2(t)$ ,  $t \in (-\infty, 0)$ . In continuum coordinates, we can first write down the commutator matrix,

$$\mathbf{K} = \begin{bmatrix} \mathbf{K}^B & & \\ & \mathbf{K}^A & \\ & & \mathbf{K}^V \end{bmatrix}, \quad (\text{D1})$$

with

$$\mathbf{K}^A = \mathbf{K}^B = \begin{bmatrix} 0 & i \\ -i & 0 \end{bmatrix}, \quad \mathbf{K}^V = \begin{bmatrix} 0 & i\delta(t-t') \\ -i\delta(t-t') & 0 \end{bmatrix}. \quad (\text{D2})$$

Note that  $\mathbf{K}^V$  is a  $2 \times 2$  block matrix, but each block is infinite dimensional, with columns and rows indexed by  $t$  and  $t'$ , respectively. The indices  $t$  and  $t'$  each run through all negative real numbers,  $(-\infty, 0]$ . In order to represent these covariance matrices in a less ambiguous and more operational way, we shall adopt an index notation, in which  $j, k, l, m$  are discrete and run through 1 and 2, while  $t$  and  $t'$  are continuous and run through negative real numbers. We can then write

$$K_{jk}^A = i\epsilon_{jk}, \quad K_{lm}^B = i\epsilon_{lm}, \quad K_{lt,mt'}^V = i\epsilon_{lm}\delta(t-t'). \quad (\text{D3})$$

Note that for  $\mathbf{K}^V$  we have a two-dimensional row index  $(l, t)$ , as well as a two-dimensional column index  $(m, t')$ , to label quadrature and arrival time.

The covariance matrix  $\mathbf{V}$  of the system contains the steady state correlations between the mechanical mode at  $t = 0$ , the cavity mode at  $t = 0$ , and the outgoing light field modes for  $t < 0$ . It can be written as

$$\mathbf{V} = \begin{bmatrix} V^{BB} & V^{BA} & V^{Bv} \\ V^{AB} & V^{AA} & V^{Av} \\ V^{vB} & V^{vA} & V^{vv} \end{bmatrix} \equiv \begin{bmatrix} V^{QQ} & V^{Qv} \\ V^{vQ} & V^{vv} \end{bmatrix}. \quad (\text{D4})$$

Here each of  $A$  and  $B$  represent two dimensions, while  $v$  represents an infinite number of dimensions. For computational purposes we can group  $A$  and  $B$  together as  $Q$ , or

$$\hat{Q}_J = \hat{Q}_{(1,2,3,4)} = (\hat{B}_1, \hat{B}_2, \hat{A}_1, \hat{A}_2). \quad (\text{D5})$$

Here we shall use upper-case Latin indices to run from 1 to 4, to label quadratures in the mechanical and cavity modes. We can write

$$V_{JK}^{QQ} = \frac{1}{2} \langle \hat{Q}_J \hat{Q}_K + \hat{Q}_K \hat{Q}_J \rangle = \frac{1}{2} \int_{-\infty}^{+\infty} \frac{d\Omega}{2\pi} S_{Q_J Q_K}(\Omega), \quad (\text{D6})$$

where the (one-sided) cross spectrum is defined via

$$\frac{1}{2} S_{XY}(\Omega) \delta(\Omega - \Omega') = \frac{1}{2} \langle \hat{X}(\Omega) \hat{Y}^\dagger(\Omega') + \hat{Y}^\dagger(\Omega') \hat{X}(\Omega) \rangle, \quad (\text{D7})$$

and they can be obtained from solutions to the Heisenberg Equations, as well as the spectra

$$S_{u_i u_j}(\Omega) = \delta_{ij}, \quad (\text{D8})$$

and the prescriptions we use for the spectra of  $S_{n_X}(\Omega)$  and  $S_{n_F}(\Omega)$ . The uncorrelated white spectra between  $\hat{u}_1$  and  $\hat{u}_2$  in Eq. (D8) result from the ingoing light field being in its vacuum state. We shall discuss the magnitude and frequency dependence of  $S_{n_X}(\Omega)$  and  $S_{n_F}(\Omega)$  in depth in the next section.

For elements that involve  $v$ , we shall still use  $lt$  for column indices and  $mt'$  for row indices. We then have

$$\begin{aligned} V_{J,mt'}^{Qv} &= \frac{1}{2} \langle \hat{Q}_J \hat{v}_m(t') + \hat{v}_m(t') \hat{Q}_J \rangle \\ &= \frac{1}{2} \int_{-\infty}^{+\infty} \frac{d\Omega}{2\pi} S_{Q_J v_m}(\Omega) e^{i\Omega t'}, \end{aligned} \quad (\text{D9})$$

and

$$\begin{aligned} V_{lt,mt'}^{vv} &= \frac{1}{2} \langle \hat{v}_l(t) \hat{v}_m(t') + \hat{v}_m(t) \hat{v}_l(t') \rangle \\ &= \frac{1}{2} \int_{-\infty}^{+\infty} \frac{d\Omega}{2\pi} S_{v_l v_m}(\Omega) e^{-i\Omega(t-t')}. \end{aligned} \quad (\text{D10})$$

Note that  $V_{J,mt'}^{Qv} = V_{mt',J}^{vQ}$ .

In numerical computations, we will have to convert the continuum of  $t, t' \leq 0$  into a finite grid. This means we will sample a finite duration  $T$  with a step size of  $\Delta t$ . We shall still use lower-case Latin indices to run from 1 to 2, and upper case Latin indices to run from 1 to 4, while use Greek indices, for

example,  $\alpha = 0, 1, 2, \dots, T/\Delta t \equiv \mathcal{N} - 1$  to replace  $t$ . We shall write

$$K_{lt,mt'}^{vv} \rightarrow K_{l\alpha,m\alpha'}^{vv} = i\epsilon_{lm} \delta_{\alpha\alpha'}. \quad (\text{D11})$$

Note that a Kronecker delta now replaces the Dirac delta. For the covariance matrix, we replace

$$V_{J,mt'}^{Qv} \rightarrow V_{J,m\alpha'}^{Qv} = \frac{\sqrt{\Delta t}}{2} \langle \hat{Q}_J \hat{v}_m(t_{\alpha'}) + \hat{v}_m(t_{\alpha'}) \hat{Q}_J \rangle, \quad (\text{D12})$$

which are  $4 \times 2\mathcal{N}$  and  $2\mathcal{N} \times 4$  dimensional matrices (with  $V_{J,mt'}^{vQ}$ ), and

$$V_{lt,mt'}^{vv} \rightarrow V_{l\alpha,m\alpha'}^{vv} = \frac{\Delta t}{2} \langle \hat{v}_l(t_\alpha) \hat{v}_m(t_{\alpha'}) + \hat{v}_m(t_\alpha) \hat{v}_l(t_{\alpha'}) \rangle, \quad (\text{D13})$$

which is a  $2\mathcal{N} \times 2\mathcal{N}$ -dimensional matrix. For the discrete sampling times we have defined

$$t_\alpha = -\left(\alpha + \frac{1}{2}\right)\Delta t, \quad (\text{D14})$$

where the additional  $\frac{1}{2}\Delta t$  provides a faster convergence in numerics. The entire covariance matrix is then  $(2\mathcal{N}+4) \times (2\mathcal{N}+4)$ -dimensional.

Our particular convention of inserting  $\Delta t$  at various places of the matrix is associated with our convention of discretizing vectors. For a generic variable, in the continuum form, we can always express it as

$$\begin{aligned} X &= \alpha^j \hat{A}_j + \beta^j \hat{B}_j + \int_{-\infty}^0 \xi^j(t) \hat{v}_j(t) dt \\ &= \gamma^J \hat{Q}_J + \int_{-\infty}^0 \xi^j(t) \hat{v}_j(t) dt, \end{aligned} \quad (\text{D15})$$

where we have used upper indices for vector components, and have grouped  $\alpha^j$  and  $\beta^j$  into  $\gamma^J$ . The variance of  $X$ , which is formally written as  $\mathbf{X}^\dagger \mathbf{V} \mathbf{X}$ , will then be

$$\begin{aligned} \mathbf{X}^\dagger \mathbf{V} \mathbf{X} &= \frac{1}{2} \gamma^J \langle \hat{Q}_J \hat{Q}_K + \hat{Q}_K \hat{Q}_J \rangle \gamma^K \\ &+ \int_{-\infty}^0 \gamma^J \langle \hat{Q}_J \hat{v}_m(t') + \hat{v}_m(t') \hat{Q}_J \rangle \xi^m(t') dt' \\ &+ \frac{1}{2} \iint_{-\infty}^0 \xi^l(t) \langle \hat{v}_l(t) \hat{v}_m(t') + \hat{v}_m(t) \hat{v}_l(t') \rangle \xi^m(t') dt dt'. \end{aligned} \quad (\text{D16})$$

As we convert the integrals in Eq. (D16) into summations,  $\int$  will become  $\Sigma$ , while  $dt$  will become  $\Delta t$ . We shall take

$$\xi^{m\alpha} = \xi^m(t_\alpha) \sqrt{\Delta t}. \quad (\text{D17})$$

Together with Eq. (D12)–(D13), the fully discretized version of Eq. (D16) will then be

$$\begin{aligned} \mathbf{X}^\dagger \mathbf{V} \mathbf{X} &= \gamma^J V_{JK}^{QQ} \gamma^K + \gamma^J V_{J,m\alpha}^{Qv} \xi^{m\alpha} + \xi^{l\beta} V_{l\beta,K}^{vQ} \gamma^K \\ &+ \xi^{l\alpha} V_{l\alpha,m\beta}^{vv} \xi^{m\beta}. \end{aligned} \quad (\text{D18})$$

In this convention, the usual vector norm for the discretized version of a function of time coincides with the  $L^2$ -norm of that function. It can also be checked that discretized matrices in Eqs. (D11)–(D13), when contracted with vectors in this convention, lead to the appropriate integrals. Note that if a  $\delta(t_\alpha - t'_\alpha)$  shows up in Eq. (D13), we will take  $\Delta t \delta(t_\alpha - t'_\alpha) \rightarrow \delta_{\alpha\alpha'}$ , as in Eq. (D11).

Corresponding to the discussion at the end of Sec. III (also shown in Fig. 1), here we consider entanglement between: (i) mass at  $t = 0$  and the out-going light field that had emerged during  $t \leq 0$  and (ii) mass and the joint system of the cavity mode as well as light that had emerged during  $t \leq 0$ . In case (i), we simply throw away elements involving  $A$  in both  $\mathbf{K}$  and  $\mathbf{V}$ , while in case (ii) we consider the full matrices. In both cases,  $\mathbf{V}_{\text{pt}}$  is obtained by adding a minus sign to the column involving  $\hat{B}_2$  and the row involving  $\hat{B}_2$  – but not the diagonal element at which they intersect.

### Appendix E: Numerical Implementation for aLIGO's Noise

In our simulations, we use  $dt = 0.25$  ms and  $T = 0.1$  s, which corresponds to sampling the light field at 4000 Hz and working with the outgoing field emitted from the cavity between  $t = -0.1$  s and  $t = 0$  s. We achieve numerical convergence with these parameters. To quantify the amount of entanglement in the system, we use the logarithmic negativity defined in Eq. (14). However, this is possible only for low levels of classical noise. For high levels of classical noise, classical correlations dominate over quantum correlations, which causes the cross-correlation values in the system to cover a wide-range of orders of magnitude, mostly due to the 14th power of  $\Omega$  in our force noise model Eq. (18). For aLIGO parameters, the entries of the covariance matrix span about 20 orders of magnitudes, while we attempt to find a symplectic eigenvalue of order 1 – this is numerically an extremely challenging problem.

Numerical errors also arise because of time-binning with an insufficient resolution. Thus, we lose precision on the numerically determined covariance matrices. This affects the smallest symplectic eigenvalue  $\tilde{\nu}_{\min}$  to the point that it cannot be used to measure entanglement with the logarithmic negativity. Numerical imprecision can lead to covariance matrices that do not satisfy Heisenberg uncertainty bound Eq. (12), they thus do not correspond to a bona fide state and we call them *non-physical*. One way to get around this loss of precision is to use the PPT criterion as a yes/no test only, renouncing the magnitude information of  $\tilde{\nu}_{\min}$ . The sampling frequency during time binning should be higher than the Nyquist rate of the system (i.e. twice the largest frequency in the system), since the entries of the covariance matrix contain correlations from all frequencies. In our system, the largest frequency is the cavity decay rate  $\gamma = 424$  Hz. Therefore, we choose  $dt < 1/(2 \cdot 424) \approx 1.2$  ms. However, as we decrease  $dt$ , we are limited by computational resources, such as the RAM size, or time. The parameter  $dt$  is limited to an optimal range determined by this trade-off. We thus develop the following strategy: we first quantify the amount of numerical errors in

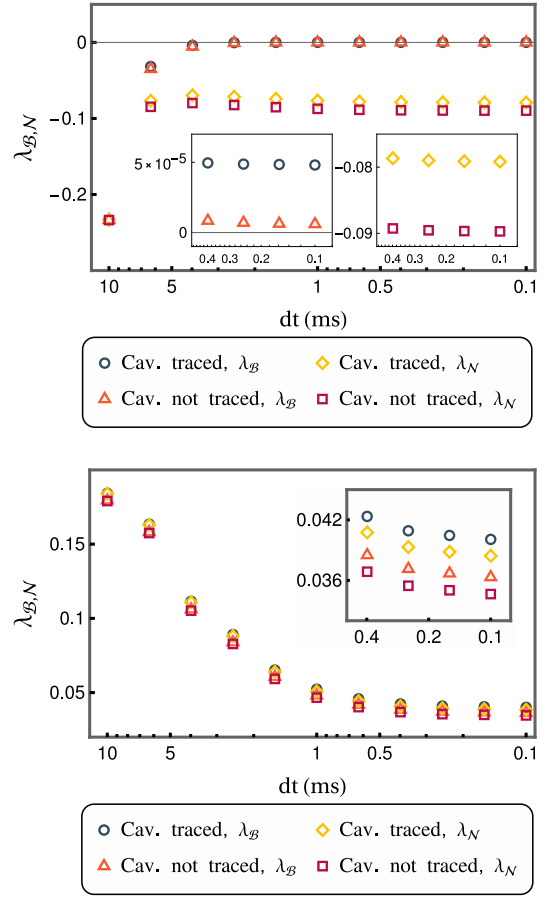


FIG. E.1.  $\lambda_B$  and  $\lambda_N$  for  $\alpha_{F_1} = 10^{-15}$  and  $\alpha_{F_2} = 15$  (top row, Figure a),  $\alpha_{F_1} = 10^{-8}$ ,  $\alpha_{F_2} = 10$ , and  $\alpha_{X_2} = 10^3$  (bottom row, Figure b). We set  $T = 0.1$  s, and  $dt \in [0.1, 10]$  ms. Note that  $dt$  decreases to the right of the plots. In Figure a, entanglement exists for both partitions, and  $\lambda_B(\lambda_N)$  is re-plotted in the inset on the left(right) for  $dt \in [0.1, 0.5]$  ms. In Figure b, the state is separable for both partitions, and  $\lambda_B$  and  $\lambda_N$  are re-plotted in the inset for  $dt \in [0.1, 0.5]$  ms.

the system by computing the most negative eigenvalue (if it exists) of  $\mathbf{V} + \frac{1}{2}\mathbf{K}$  before and after the partial transpose operation, denoted as  $\lambda_B$  and  $\lambda_N$  respectively. Then, we decide that entanglement exists if  $\lambda_B > 0$  and  $\lambda_N < 0$ , or if  $\lambda_B < 0$  and  $|\lambda_N| \gg |\lambda_B|$ . Furthermore, we decide that the system is separable if  $\lambda_B > 0$  and  $\lambda_N > 0$ .

Two case studies about this strategy can be found in Fig. E.1 where we fix  $T = 0.1$  s, change  $dt$ , and examine how  $\lambda_N$  and  $\lambda_B$  change by plotting  $\lambda_N$  and  $\lambda_B$ . We decide on entanglement if  $\lambda_B \geq 0$  and  $\lambda_N < 0$ , or  $\lambda_B < 0$ ,  $\lambda_N < 0$ , and  $|\lambda_N| \geq 100|\lambda_B|$ . Our criteria for convergence is a relative change smaller than 5% for both  $\lambda_N$  and  $\lambda_B$  as we change  $dt$ . In Fig. E.1a, we work with a low level of classical force noise and set  $\alpha_{F_1} = 10^{-15}$ ,  $\alpha_{F_2} = 15$  in Eq. (18). We see that  $\lambda_N$  and  $\lambda_B$  converge with  $\lambda_N$  changing by 0.053%, 0.068%, and  $\lambda_B$  changing by 4.9%, 0.77% before and after tracing over the cavity respectively, for  $dt = 0.1$  ms. The system is entangled for both partitions since  $\lambda_B \geq 0$  and  $\lambda_N < 0$ . Furthermore,  $\lambda_B$  becomes positive and converges after  $dt \sim 1$  ms, or a sampling frequency of 1000 Hz; consistent with the discussion

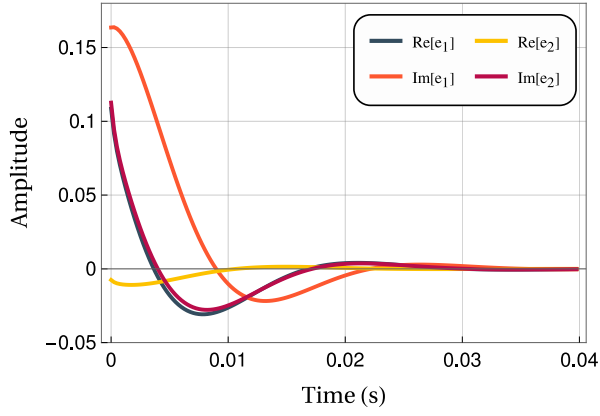


FIG. E.2. The real and imaginary parts of the eigenvector for the negative eigenvalue of  $\mathbf{V}_{\text{pt}} + \frac{1}{2}\mathbf{K}$  for  $\alpha_{F_1} = 10^{-15}$ ,  $\alpha_{F_2} = 15$ , denoted by  $e_1$  and  $e_2$ , which correspond to the first and second halves of the entire eigenvector respectively. The reason behind this slicing is the block-matrix structure of the light-field sector of the covariance matrix. Furthermore, since the light field modes are continuous in time,  $e_1$  and  $e_2$  are also functions of time.

above relating physicality to Nyquist rate of  $\sim 850$  Hz. We also see that  $\lambda_N$  converges for similar values of  $dt$  from Fig. E.1a.

In Fig. E.2, we plot the light-field section of the eigenvector associated to the (converged) minimal eigenvalue of  $\mathbf{V}_{\text{pt}} + \frac{1}{2}\mathbf{K}$ , for the partition where we do not trace over the cavity and with  $\alpha_{F_1} = 10^{-15}$ ,  $\alpha_{F_2} = 15$ . It corresponds to a temporal mode of the free electromagnetic field outside the cavity. It is that particular mode associated to the (sole) negative eigenvalue that is entangled with the joint system mechanics plus cavity. The four curves correspond to the real and imaginary parts of the  $\hat{v}_1(t)$  and  $\hat{v}_2(t)$ . They have the form of smooth decaying oscillations with the same frequency and decay rate, but differing by a phase. This form of the mode functions was predicted for a white force noise in [6]; which gives us confidence in the correctness of our study. Also, exponentially decaying demodulation pulses were used to demonstrate optomechanical entanglement [8, 16] and proposed for a demonstration in the stationary regime [23]. We fit functions in the form of  $e^{-\gamma_* t} \sin(\omega_* t + \theta)$  to each curve, which results in  $\omega_*/(2\pi) \approx 40$  Hz, and  $\gamma_*/(2\pi) \approx 25$  Hz. In the frequency domain, exponentially decaying harmonic oscillations are Lorentzians, centered at  $\pm\omega_*$  and with a bandwidth (FWHM)  $2\gamma_*$ . In aLIGO's noise budget (Fig. 3), these Lorentzians are on the low frequency side of the low-noise band and their HWHM to the left crosses the quantum noise, where it is not yet dominated by suspension thermal and seismic noises – although we saw in Sec. VI A that the latter is probably the main mechanism preventing optomechanical entanglement. We add that Lorentzians are heavy-tail distributions, being a possible reason why even lower frequency components matter.

In Fig. E.1b, we set  $\alpha_{F_1} = 10^{-8}$ ,  $\alpha_{F_2} = 10$ , and  $\alpha_{X_2} = 10^3$ , causing the sensing noise to dominate over quantum noise for frequencies in the 30 – 2000 Hz band. We again see that  $\lambda_N$  and  $\lambda_B$  converge with  $\lambda_N$  changing by 1.3%, 1.2%, and  $\lambda_B$  changing by 1.2%, 1.1% before and after tracing over the cav-

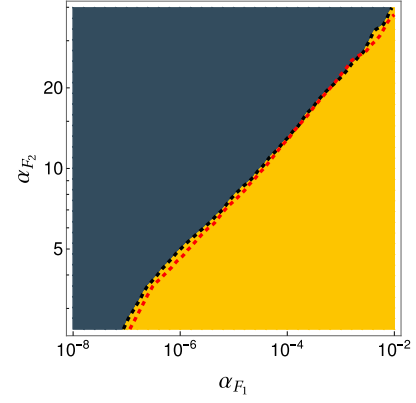


FIG. E.3. Contour plot depicting the effect of the force noise spectrum on our numerical precision for both partitions. The force noise levels increase toward the bottom-right of the figure. The black and the red dashed lines separate the regions where numerics converge from the regions where numerics fail for the partition where we do and do not trace over the cavity respectively. The region where numerics converge for both partitions is marked in gray, whereas numerics fail for both partitions toward the bottom right of the figure, past the red dashed line, in the yellow region.

ity respectively, for  $dt = 0.1$  ms. Since  $\lambda_B$  and  $\lambda_N$  are positive for both partitions, we conclude that there is no entanglement in the system for either partition. When we increase the classical noise level we see that convergence is much harder to achieve. Furthermore,  $\lambda_B$  and  $\lambda_N$  are negative, and  $\lambda_B \sim \lambda_N$  for every value of  $dt$  regardless of when we do or do not trace over the cavity. Therefore, we cannot conclude that there is entanglement for neither of the partitions. These case studies show that we can use  $\lambda_B$  as an indicator of the “non-physicality” of the covariance matrix  $\mathbf{V}$  introduced by finite-sampling and high levels of classical noise in the system, and that the negativity of  $\lambda_N$  is not enough to decide on entanglement when we consider the numerics.

For our model of aLIGO's non-Markovian noises, Eqs. (18), we study the numerical stability of broad noise regimes, parametrized by the pair  $\alpha_{F_j}$ ,  $j = 1, 2$ . We set  $\alpha_{X_j} = 1$ ,  $j = 1, 2$ , since we saw that force noise had a greater impact on numerical stability than sensing noise in our simulations for aLIGO's noise. In Fig. E.3, we plot the boundary between noise regimes where the numerics converge and the computed covariance matrices are physical (in gray) and those regimes where the numerics fail (either at converging or at generating physical covariance matrices or both) with the available computing resources (in yellow). As a matter of fact, in all the operation regimes in the gray region where the numerics work, the system is entangled. This means that our model predicts optomechanical entanglement in aLIGO, if its classical noise is in this gray region. Recall that the current status of aLIGO corresponds to  $\alpha_{F_j} = \alpha_{X_j} = 1$ ,  $j = 1, 2$ , far to the bottom-right in the undecidable yellow region.

If we follow the red dashed line in Fig. E.3, we continuously sample the force noise spectrum over the boundary where our numerics converge, and the system is entangled, for the partition where we do not trace over the cavity.

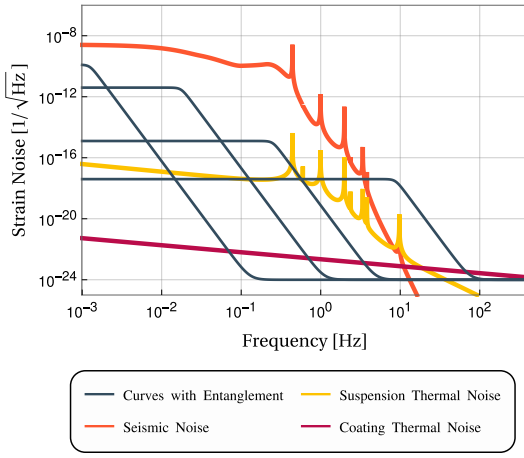


FIG. E.4. Examples of force noise spectra along the boundary where we lose numerical precision (defined with  $|\lambda_N| = 100|\lambda_B|$ ) for the partition where we do not trace over the cavity, plotted in black. aLIGO noise curves are also plotted for comparison. The black curves are parametrized with (from left to right)  $\alpha_{F_1} = 1$  and  $\alpha_{F_2} = 200$ ,  $\alpha_{F_1} = 10^{-3}$  and  $\alpha_{F_2} = 14$ ,  $\alpha_{F_1} = 10^{-10}$  and  $\alpha_{F_2} = 1$ , and  $\alpha_{F_1} = 10^{-15}$  and  $\alpha_{F_2} = 0.029$ .

This boundary corresponds to a lower limit of the maximum amount of classical noise allowed in the system in order to have entanglement. We plot some of these noise curves in Fig. E.4. Note that if we set  $\alpha_{F_1}$  or  $\alpha_{F_2}$  to be unity, the corresponding pairs of  $\alpha_{F_1}$ ,  $\alpha_{F_2}$  situated on this boundary would be  $\alpha_{F_1} = 1$  and  $\alpha_{F_2} \geq 200$ , or for  $\alpha_{F_2} = 1$  and  $\alpha_{F_1} \leq 10^{-10}$ . The corresponding noise curves are also plotted on Fig. E.4.

- 
- [1] C. Genes, A. Mari, D. Vitali, and P. Tombesi, Chapter 2 quantum effects in optomechanical systems, in *Advances in Atomic Molecular and Optical Physics*, Advances In Atomic, Molecular, and Optical Physics, Vol. 57 (Academic Press, 2009) pp. 33–86.
  - [2] S. G. Hofer and K. Hammerer, Entanglement-enhanced time-continuous quantum control in optomechanics, *Phys. Rev. A* **91**, 033822 (2015).
  - [3] C. Genes, A. Mari, P. Tombesi, and D. Vitali, Robust entanglement of a micromechanical resonator with output optical fields, *Phys. Rev. A* **78**, 032316 (2008).
  - [4] H. Miao, S. Danilishin, H. Müller-Ebhardt, and Y. Chen, Achieving ground state and enhancing optomechanical entanglement by recovering information, *New Journal of Physics* **12**, 083032 (2010).
  - [5] H. Miao, S. Danilishin, H. Müller-Ebhardt, H. Rehbein, K. Somiya, and Y. Chen, Probing macroscopic quantum states with a sub-heisenberg accuracy, *Phys. Rev. A* **81**, 012114 (2010).
  - [6] H. Miao, S. Danilishin, and Y. Chen, Universal quantum entanglement between an oscillator and continuous fields, *Physical Review A* **81**, 10.1103/physreva.81.052307 (2010).
  - [7] S. L. Danilishin, F. Y. Khalili, and H. Miao, Advanced quantum techniques for future gravitational-wave detectors, *Living Reviews in Relativity* **22**, 10.1007/s41114-019-0018-y (2019).
  - [8] S. G. Hofer, W. Wieczorek, M. Aspelmeyer, and K. Hammerer, Quantum entanglement and teleportation in pulsed cavity optomechanics, *Phys. Rev. A* **84**, 052327 (2011).
  - [9] M. Aspelmeyer, T. J. Kippenberg, and F. Marquardt, Cavity optomechanics, *Reviews of Modern Physics* **86**, 1391 (2014).
  - [10] S. Barzanjeh, E. S. Redchenko, M. Peruzzo, M. Wulf, D. P. Lewis, G. Arnold, and J. M. Fink, Stationary entangled radiation from micromechanical motion, *Nature* **570**, 480 (2019).
  - [11] J. Chen, M. Rossi, D. Mason, and A. Schliesser, Entanglement of propagating optical modes via a mechanical interface, *Nature Communications* **11**, 943 (2020).
  - [12] R. Riedinger, A. Wallucks, I. Marinković, C. Löschnauer, M. Aspelmeyer, S. Hong, and S. Gröblacher, Remote quantum entanglement between two micromechanical oscillators, *Nature* **556**, 473 (2018).
  - [13] C. F. Ockeloen-Korppi, E. Damskägg, J.-M. Pirkkalainen, M. Asjad, A. A. Clerk, F. Massel, M. J. Woolley, and M. A. Sillanpää, Stabilized entanglement of massive mechanical oscillators, *Nature* **556**, 478 (2018).
  - [14] S. Kotler, G. A. Peterson, E. Shojaei, F. Lecocq, K. Cicak, A. Kwiatkowski, S. Geller, S. Glancy, E. Knill, R. W. Simmonds, J. Aumentado, and J. D. Teufel, Direct observation of deterministic macroscopic entanglement, *Science* **372**, 622 (2021).
  - [15] R. A. Thomas, M. Parniak, C. Østfeldt, C. B. Møller, C. Bærentsen, Y. Tsaturyan, A. Schliesser, J. Appel, E. Zeuthen, and E. S. Polzik, Entanglement between distant macroscopic mechanical and spin systems, *Nature Physics* **17**, 228 (2021).
  - [16] T. A. Palomaki, J. D. Teufel, R. W. Simmonds, and K. W. Lehnert, Entangling mechanical motion with microwave fields, *Science* **342**, 710 (2013), <https://www.science.org/doi/pdf/10.1126/science.1244563>.
  - [17] O. Romero-Isart, Quantum superposition of massive objects and collapse models, *Phys. Rev. A* **84**, 052121 (2011).
  - [18] H. Müller-Ebhardt, H. Rehbein, R. Schnabel, K. Danzmann, and Y. Chen, Entanglement of macroscopic test masses and the standard quantum limit in laser interferometry, *Phys. Rev. Lett.* **100**, 013601 (2008).
  - [19] R. Schnabel, Einstein-podolsky-rosen-entangled motion of two massive objects, *Phys. Rev. A* **92**, 012126 (2015).
  - [20] M. Wang, X.-Y. Lü, Y.-D. Wang, J. Q. You, and Y. Wu, Macroscopic quantum entanglement in modulated optomechanics, *Phys. Rev. A* **94**, 053807 (2016).
  - [21] S. Pirandola, D. Vitali, P. Tombesi, and S. Lloyd, Macroscopic entanglement by entanglement swapping, *Phys. Rev. Lett.* **97**,

- 150403 (2006).
- [22] M. Ludwig, K. Hammerer, and F. Marquardt, Entanglement of mechanical oscillators coupled to a nonequilibrium environment, *Phys. Rev. A* **82**, 012333 (2010).
  - [23] C. Gut, K. Winkler, J. Hoelscher-Obermaier, S. G. Hofer, R. M. Nia, N. Walk, A. Steffens, J. Eisert, W. Wieczorek, J. A. Slater, M. Aspelmeyer, and K. Hammerer, Stationary optomechanical entanglement between a mechanical oscillator and its measurement apparatus, *Phys. Rev. Res.* **2**, 033244 (2020).
  - [24] D. Vitali, S. Gigan, A. Ferreira, H. R. Böhm, P. Tombesi, A. Guerreiro, V. Vedral, A. Zeilinger, and M. Aspelmeyer, Optomechanical entanglement between a movable mirror and a cavity field, *Phys. Rev. Lett.* **98**, 030405 (2007).
  - [25] M. Paternostro, D. Vitali, S. Gigan, M. S. Kim, C. Brukner, J. Eisert, and M. Aspelmeyer, Creating and probing multipartite macroscopic entanglement with light, *Phys. Rev. Lett.* **99**, 250401 (2007).
  - [26] V. Giovannetti and D. Vitali, Phase-noise measurement in a cavity with a movable mirror undergoing quantum brownian motion, *Phys. Rev. A* **63**, 023812 (2001).
  - [27] S. Fedorov, V. Sudhir, R. Schilling, H. Schütz, D. Wilson, and T. Kippenberg, Evidence for structural damping in a high-stress silicon nitride nanobeam and its implications for quantum optomechanics, *Physics Letters A* **382**, 2251 (2018), special Issue in memory of Professor V.B. Braginsky.
  - [28] S. Gröblacher, A. Trubarov, N. Prigge, G. D. Cole, M. Aspelmeyer, and J. Eisert, Observation of non-markovian micromechanical brownian motion, *Nature Communications* **6**, 7606 (2015).
  - [29] J. Aasi *et al.*, Advanced ligo, *Classical and Quantum Gravity* **32**, 074001 (2015).
  - [30] H. Yu and members of the LIGO Scientific Collaboration, Quantum correlations between light and the kilogram-mass mirrors of ligo, *Nature* **583**, 43 (2020).
  - [31] The quantum noise's beating of the SQL is only inferred by subtracting a classical noise floor that was obtained through calibration.
  - [32] A. Buonanno and Y. Chen, Scaling law in signal recycled laser-interferometer gravitational-wave detectors, *Physical Review D* **67**, 10.1103/physrevd.67.062002 (2003).
  - [33] Y. Chen, Macroscopic quantum mechanics: theory and experimental concepts of optomechanics, *Journal of Physics B: Atomic, Molecular and Optical Physics* **46**, 104001 (2013).
  - [34] We use the convention  $\mathcal{F}\{f(t)\} = \int_{-\infty}^{\infty} f(t)e^{i\omega t} dt$ .
  - [35] C. M. Caves and B. L. Schumaker, New formalism for two-photon quantum optics. i. quadrature phases and squeezed states, *Phys. Rev. A* **31**, 3068 (1985).
  - [36] B. L. Schumaker and C. M. Caves, New formalism for two-photon quantum optics. ii. mathematical foundation and compact notation, *Phys. Rev. A* **31**, 3093 (1985).
  - [37] S. L. Danilishin and F. Y. Khalili, Quantum measurement theory in gravitational-wave detectors, *Living Reviews in Relativity* **15**, 10.12942/lrr-2012-5 (2012).
  - [38] R. Kubo, The fluctuation-dissipation theorem, *Reports on progress in physics* **29**, 255 (1966).
  - [39] H. J. Kimble, Y. Levin, A. B. Matsko, K. S. Thorne, and S. P. Vyatchanin, Conversion of conventional gravitational-wave interferometers into quantum nondemolition interferometers by modifying their input and/or output optics, *Physical Review D* **65**, 10.1103/physrevd.65.022002 (2001).
  - [40] A. Peres, Separability criterion for density matrices, *Phys. Rev. Lett.* **77**, 1413 (1996).
  - [41] G. Adesso and F. Illuminati, Entanglement in continuous-variable systems: recent advances and current perspectives, *Journal of Physics A: Mathematical and Theoretical* **40**, 7821 (2007).
  - [42] R. F. Werner and M. M. Wolf, Bound entangled gaussian states, *Phys. Rev. Lett.* **86**, 3658 (2001).
  - [43] R. Simon, Peres-horodecki separability criterion for continuous variable systems, *Phys. Rev. Lett.* **84**, 2726 (2000).
  - [44] G. Vidal and R. F. Werner, Computable measure of entanglement, *Phys. Rev. A* **65**, 032314 (2002).
  - [45] A. Serafini, *Quantum Continuous Variables* (CRC Press, 2017).
  - [46] V. B. Braginsky, F. Y. Khalili, and K. S. Thorne, *Quantum Measurement* (Cambridge University Press, 1992).
  - [47] P. R. Saulson, Thermal noise in mechanical experiments, *Phys. Rev. D* **42**, 2437 (1990).
  - [48] G. I. González and P. R. Saulson, Brownian motion of a torsion pendulum with internal friction, *Physics Letters A* **201**, 12 (1995).
  - [49] A. R. Neben, T. P. Bodiya, C. Wipf, E. Oelker, T. Corbitt, and N. Mavalvala, Structural thermal noise in gram-scale mirror oscillators, *New Journal of Physics* **14**, 115008 (2012).
  - [50] The spectrum of the mechanical displacement per unit Hz, where the transduction of the force and sensing noises by the cavity is effectively factored out.
  - [51] To find spectra of the form of Eqs. (16), one assumes the free-mass and high- $Q$  limits where the mechanical susceptibility behaves as  $1/\Omega^2$ ; additionally, one must be in frequency ranges where the noise spectra  $S_{nf}$  and  $S_{nx}$  are constant polynomial roll-off – typical at frequencies above the resonance of suspended oscillators.
  - [52] K. Somiya *et al.*, Detector configuration of kagra—the japanese cryogenic gravitational-wave detector, *Classical and Quantum Gravity* **29**, 124007 (2012).
  - [53] F. Acernese *et al.*, Advanced virgo: a second-generation interferometric gravitational wave detector, *Classical and Quantum Gravity* **32**, 024001 (2014).
  - [54] B. P. Abbott *et al.*, A guide to LIGO–virgo detector noise and extraction of transient gravitational-wave signals, *Classical and Quantum Gravity* **37**, 055002 (2020).
  - [55] D. V. Martynov, Hall, *et al.*, Sensitivity of the advanced ligo detectors at the beginning of gravitational wave astronomy, *Phys. Rev. D* **93**, 112004 (2016).
  - [56] S. M. Aston *et al.*, Update on quadruple suspension design for advanced ligo, *Classical and Quantum Gravity* **29**, 235004 (2012).
  - [57] Y. T. Liu and K. S. Thorne, Thermoelastic noise and homogeneous thermal noise in finite sized gravitational-wave test masses, *Phys. Rev. D* **62**, 122002 (2000).
  - [58] H. Müller-Ebhardt, H. Rehbein, C. Li, Y. Mino, K. Somiya, R. Schnabel, K. Danzmann, and Y. Chen, Quantum-state preparation and macroscopic entanglement in gravitational-wave detectors, *Physical Review A* **80**, 10.1103/physreva.80.043802 (2009).
  - [59] J. G. Rollins, E. Hall, C. Wipf, and L. McCuller, pygwinc: Gravitational Wave Interferometer Noise Calculator, *Astrophysics Source Code Library*, record ascl:2007.020 (2020), ascl:2007.020.
  - [60] G. Wanner, Space-based gravitational wave detection and how lisa pathfinder successfully paved the way, *Nature Physics* **15**, 200 (2019).